ARMA 18–1221

Hydraulic Fracture of Opalinus Shale under Uniaxial Stress: Experiment Design and Preliminary Results

AlDajani, O. A.[1], Germaine, J. T.[2], and Einstein, H. H[1]

[1]*Massachusetts Institute of Technology, Cambridge, Massachusetts, USA*

[2]*Tufts University, Medford, Massachusetts, USA*

ABSTRACT: The interaction of hydraulically induced fractures with pre-existing fractures in shales is of interest to the petroleum industry. Laboratory experiments can help to understand the fracture initiation, propagation, and coalescence behavior. A fundamental first step is to investigate the fracture interaction of a pressurized flaw (artificial crack) with a non-pressurized flaw where the specimens are subjected to a constant uniaxial stress.

This paper describes the hydraulic fracture experiment design, which allows us to pressurize an individual flaw, monitor the internal flaw pressure throughout pressurization and fracturing, and visually capture the underlying fracture mechanisms. The experiments are performed on prismatic Opalinus Shale specimens with two pre-existing flaws of various geometries. After subjecting the specimens to a constant uniaxial stress, one of the flaws is pressurized until a hydraulic fracture initiates and propagates. The interaction of the hydraulic fracture with the non-pressurized flaw is observed.

Three flaw geometries are investigated in this study: a single vertical flaw, double flaws with a step offset of 30°, and double flaws with a step offset of 60°. The first geometry was tested as a proof of concept for the experimental setup and showed the basic fracture initiation and propagation behavior. The second and third geometries capture the interaction of the hydraulic fracture with the non-pressurized flaw. Although there is only a 30° difference in the stepped angles between the two flaws, the fracture behavior is drastically different.

1. INTRODUCTION

The hydraulic fracture stimulation technique, used to enhance production from conventional reservoirs and extract trapped hydrocarbons from unconventional resources, has been developed and used for decades. However, the exact geometry of the produced hydraulic fractures remains not well known. The aim of this study is to visually capture and analyze the initiation, propagation, and interaction of hydraulic fractures with pre-existing fractures and bedding planes, and to better understand the underlying mechanisms involved.

Extensive work has been done at MIT to study fracture initiation, -propagation, and coalescence (Reyes, 1991, Bobet, 1997, Wong, 2008, Miller, 2008, Gonçalves da Silva, 2009, Morgan, 2015, Gonçalves da Silva, 2016, AlDajani, 2017). Most of these studies were done on prismatic specimens with two pre-existing artificial fractures (flaws) without the influence of hydraulic pressure (Figure 1 - a). Specimens were subjected to uniaxial compressive loading, and fracture initiation and propagation mechanisms (tensile and shear) were captured using a high-speed camera and a high-resolution camera while simultaneously measuring the stress-strain behavior. The experiments were conducted on different materials: gypsum (artificial material), marble (metamorphic rock), granite (igneous rock), and shale (sedimentary rock).

More recently, Gonçalves da Silva (2016) ran hydraulic fracture experiments on granite, where hydraulic pressure was applied to the front and rear faces of the rock, as well as in both flaws. This paper presents a new and novel experimental setup that pressurizes an individual flaw in shale to induce hydraulic fractures and to observe their interaction with a non-pressurized flaw and bedding planes (Figure 1 - b).

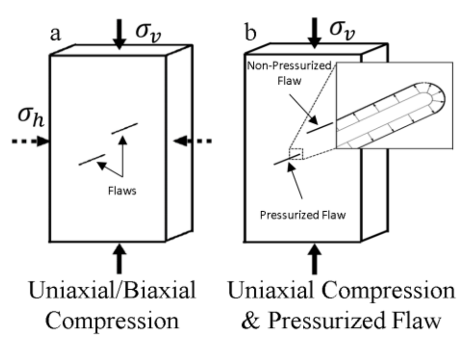

Figure 1 – a: Schematic of prismatic specimen with prefabricated flaws subject to uniaxial or biaxial loading to induce fractures and study fracture mechanisms and flaw interaction. b: Schematic of prismatic specimen subjected to a constant uniaxial load and an individual flaw pressurized to induce hydraulic fractures to study fracture mechanisms and flaw interactions. Modified from Gonçalves da Silva (2016).

The material used in this study is cored Opalinus Shale from the Underground Research Laboratory in Mont Terri, Switzerland. The mineralogy of this shale was measured using X-ray diffraction and is presented in Table 1. As shown, this is a very clay rich shale.

Table 1 – Bulk mineralogy analysis results of Opalinus Shale core sample from X-ray diffraction using Kα radiation scanning (AlDajani, 2017).

Mineral	**%**
Quartz	15.9
K-Feldspar	0.5
Plagioclase	0.9
Calcite	5.4
Dolomite	0.5
Siderite	0.3
Anatase	0.5
Apatite	1.1
Pyrite	2.2
Chlorite (Tri)	3.6
Muscovite	2
I+I/S-ML	45.4
Kaolinite	21.6

The mechanical properties were measured through unconfined compression tests and are presented in Table 2.

Table 2 – Mechanical properties of intact (no flaw) Opalinus Shale prismatic specimens subjected to unconfined compression tests (AlDajani, 2017).

	UCS, MPa	**E, MPa**	**υ**
load ⊥ to bedding	17.26	1327	0.33
load ∥ to bedding	5.76	1947	0.26

The configuration of the specimens tested is shown in Figure 2.

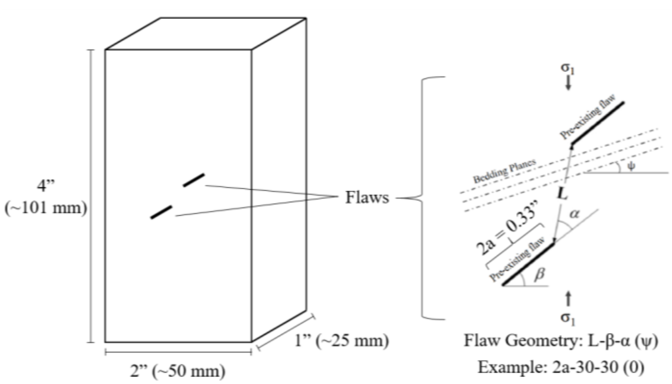

Figure 2 – Dimensions of specimens tested and flaw geometry convention. Modified from Morgan (2015).

The hydraulic fracturing process was investigated on these prismatic specimens with three different geometries:

- a single vertical flaw is tested as a proof of concept for the equipment as well as to capture hydraulic fracture initiation and propagation mechanisms.
- two stepped flaw geometries, one with a shallow bridging angle (α) and the other steeper, are tested to investigate the interaction of the hydraulic fractures with a non-pressurized flaw.

Each test was repeated three times and the results discussed are consistent throughout. The paper will now discuss the equipment (designed and fabricated at MIT), that allows one to pressurize an individual flaw with complete visual transparency. Then, the details of the experimental procedure are presented followed by a presentation of the results.

2. EXPERIMENTAL DESIGN

A novel setup was designed and built to pressurize an individual flaw and to see the fracture process.

2.1. Flaw Pressurization Device

The new flaw pressurization device is shown in Figure 3, and the numbered components are described below.

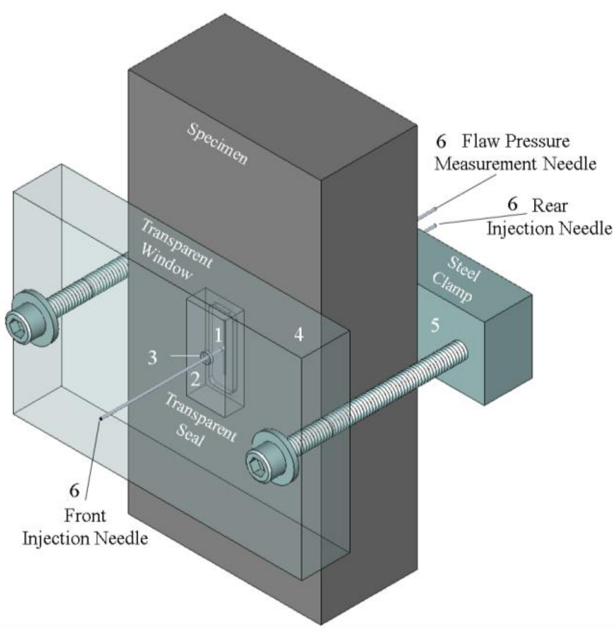

Figure 3 – Three-dimensional rendering of flaw pressurization device components (oblique front view) showing transparent polycarbonate window and flaw seal with front injection needle inserted into flaw. Note: example specimen in figure has a single vertical flaw. Other geometries possible by simply rotating flaw seal to same orientation of the pressurized flaw.

1. Transparent silicone rubber membrane (Figure 4): a transparent silicone rubber sheet is laser cut to the desired dimensions and is placed on the front and rear face of the specimen covering the flaw.

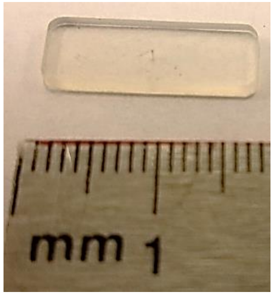

Figure 4 - Transparent silicon rubber membrane after laser-cutting from 1.6 mm thick sheet. This membrane is pressed against the specimen surface with the front injection needle passing through its center hole into the flaw. The membrane is optically transparent.

2. Transparent polycarbonate housing (Figure 5): Designed to hold the rubber seals, mentioned above, on the front and rear face of the specimen. These are rectangular polycarbonate prisms machined with a groove to hold the silicone rubber membrane on the front and an O-ring on the back with a hole in the middle for the injection needle. These are vapor polished to restore the clarity to an optical finish.

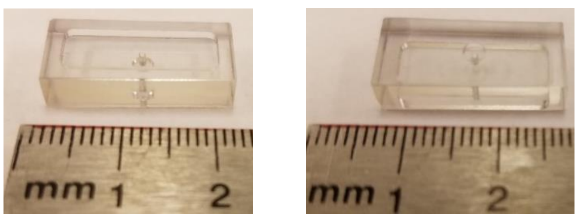

Figure 5 – Transparent polycarbonate housing after machining followed by vapor polish. Left: specimen-facing side (front) of housing where transparent membrane fits in recess. Right: outside-facing side (back) of housing where O-ring seal fits in recess.

3. O-ring seal: an O-ring is placed in the outside groove of each housing to tighten around the injection needle when compressed. It prevents the injection needle from moving and prevents injected hydraulic fluid from leaking.
4. Transparent polycarbonate window: the final component on the front of the specimen is a rectangular polycarbonate prism, wider than the specimen with two holes for the clamping bolts and a small hole in the middle for the injection needle. The window serves as the front clamp which compresses the O-ring between it and the housing, and holds the housing and seal onto the face of the specimen.
5. Steel bar clamp: a rectangular steel bar with access holes for injection needles in the middle and threated holes for the clamping bolts.
6. Needles (Figure 6): Very small diameter tubing is cut and fitted on one end to tie into pipe connecting it to the pumping apparatus while the other goes into the flaw. Two needles serve as injection needles while a third needle connects to a pressure transducer for real-time monitoring of internal flaw pressure.

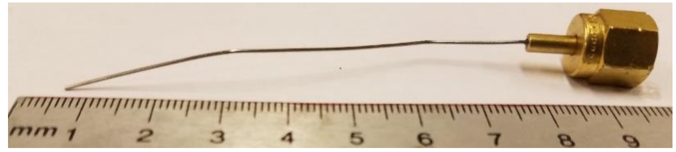

Figure 6 - Picture of needle. Needle tip passes through pressurization device components and into the flaw. Opposite end screws into copper pipe or pressure transducer.

2.2. *Experimental Procedure*

The experimental procedure has three main phases, each serving a specific purpose.

a. Application of uniaxial stress:

The specimens presented in this paper all have horizontal bedding planes. The magnitude of the uniaxial stress has to be carefully chosen to prevent unwanted fracturing.

The specimens were loaded uniaxially to 3.5 MPa at a loading rate of 4,555 N/min, and this stress was held constant. This stress was chosen to be high enough to shut the bedding planes, but low enough to not cause an external stress induced "dry" fracture.

b. Flaw saturation:

After the uniaxial stress has been applied, the front and rear injection needles (Figure 3 - component 6 and Figure 6) are tied to the pipes connecting to the pressure-volume actuator (PVA), which pumps fluid into the flaw. The PVA has a pressure transducer and linear variable differential transformer (LVDT) for pressure and volume control. To ensure all air is expelled from the flaw, the third needle is left open to atmospheric pressure. Once constant-pressure flow is established, it can be assumed that all air has been expelled from the system. At this point, the third needle is tied into a second pressure transducer, closing the system and ending the flaw saturation phase. This pressure transducer measures the flaw internal pressure throughout the test. The pressure-time behavior in the saturation process is shown in Figure 7.

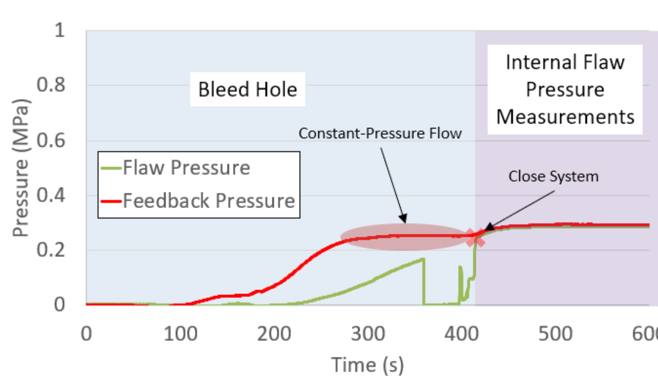

Figure 7 – Pressure-time behavior measured with the third needle during experiment setup. Saturation of the flaw occurs through the front and rear injection needles. Plot shows the third

needle initially acting as a bleed hole to fully saturate the flaw with hydraulic fluid and then closing the system with a pressure transducer to begin pressurization.

c. Pressurization:

With the specimen loaded, flaw saturated, and system closed, the test is run by pressurizing the flaw until failure. The flaw loading scheme presented in this paper is pressure controlled. This is done using a proportional-integral-derivative (PID) controller algorithm that was coded in the hydraulic pressure control computer. The user inputs a target pressure, and the closed-loop feedback PID algorithm drives the motor to achieve this target smoothly and without overshooting. A schematic of the algorithm is presented in Figure 8 with further details discussed by AlDajani (2017).

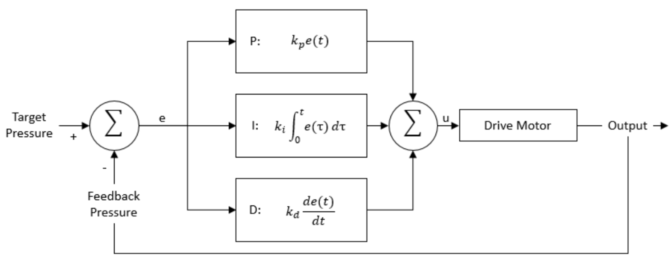

Figure 8 – Schematic of closed-loop feedback process of a PID controller.

The specimens tested in this paper were pressurized in 0.5 MPa increments until failure. Each pressure step is held for at least 1 minute. The process is recorded with a high-resolution camera taking time-lapse images every 2 seconds throughout the test, and a manually triggered high-speed camera that records the failure of the specimen at 3,000 frames per second.

The entire experimental setup is shown in Figure 9.

d. Analysis:

After the experiment, the images from the high-resolution and high-speed cameras are collected and analyzed frame by frame for detailed capture of the chronological order of crack initiation and propagation, the modes of fracturing, and the interaction of the hydraulic fractures with bedding planes, localized heterogeneities, or the non-pressurized flaw. The frames that capture these events in so called sketches are then time synchronized with the recorded pressure/volume data. Finally, each crack is traced and labeled alphabetically in chronological order, along with its mode of fracture as well as the coalescence category as classified by Wong (2008). This process is shown in Figure 8 with an example of an analyzed uniaxial compressive test on a shale specimen with co-planar flaws oriented at 30° (AlDajani et al., 2017).

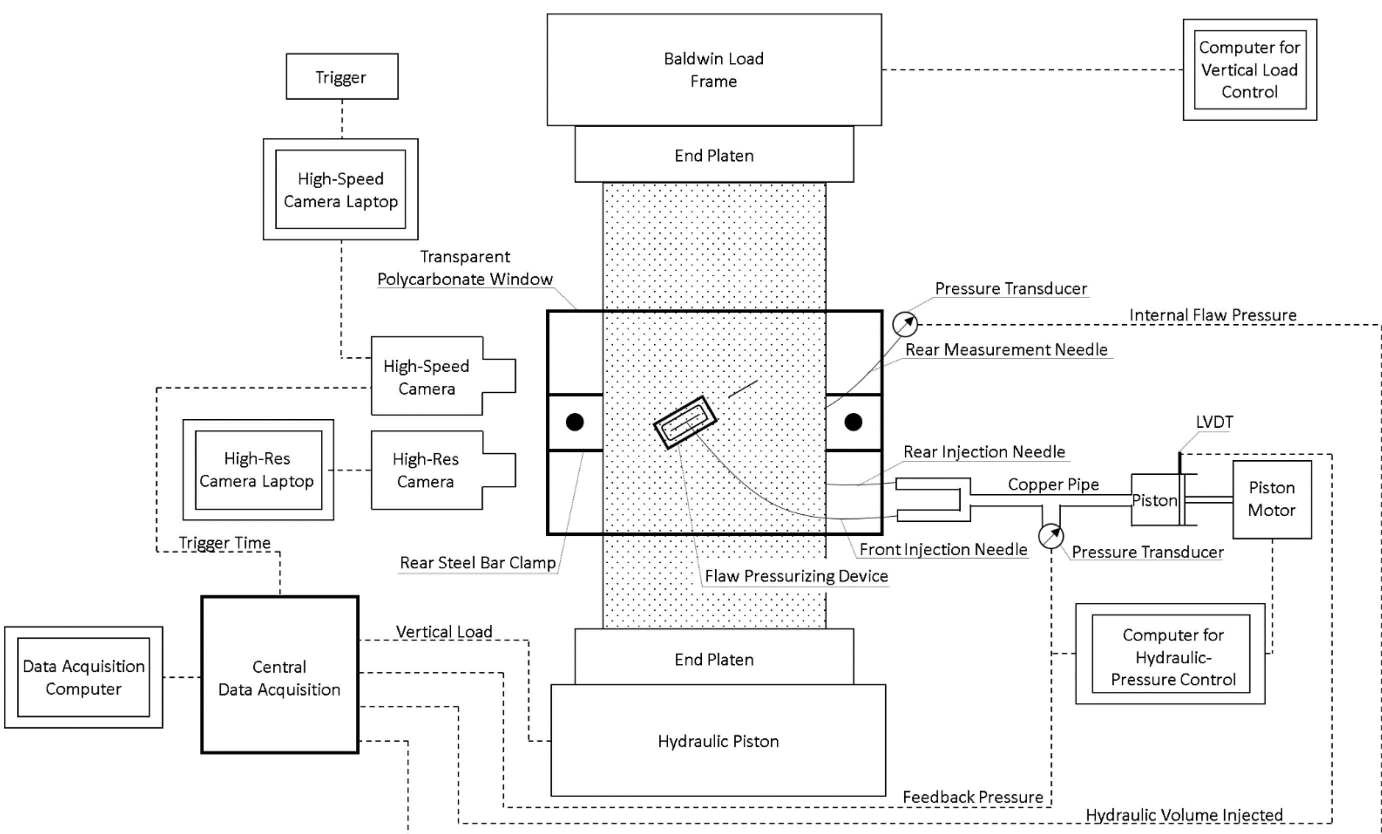

Figure 9 - Schematic of the hydraulic fracture experimental setup including the load frame, pumping equipment, imaging equipment to visually capture the hydraulic fracture process in shale, and the central data acquisition system.

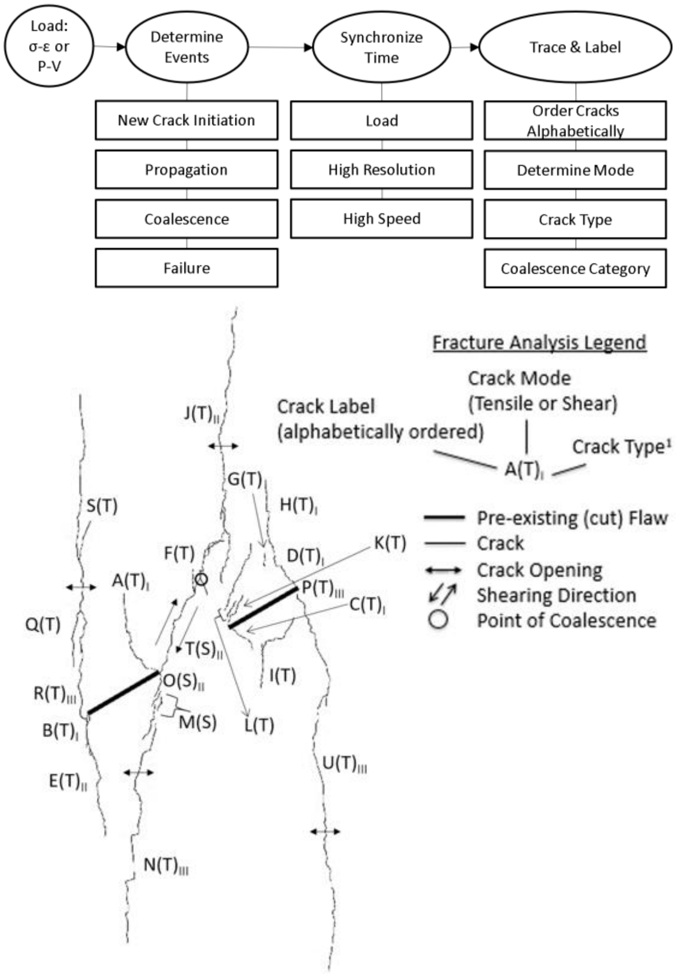

Figure 8 – Top: flow chart of experimental analysis procedure relating observed mechanisms in images to measured load data. Bottom: example of a final sketch of a uniaxial compressive test on a shale specimen with a 2a-30-0-(0) configuration showing all cracks, types ([1]:as defined by Wong, 2008), and modes (T: tensile, S: shear) (Taken from AlDajani et al., 2017)

3. RESULTS & DISCUSSION

The three flaw geometries, subjected to the hydraulic fracture experiment under uniaxial stresses described previously, are shown in Figure 9. All tested specimens contained horizontal bedding planes, were subjected to the constant uniaxial compressive stress of 3.5 MPa, and each geometry was tested three times.

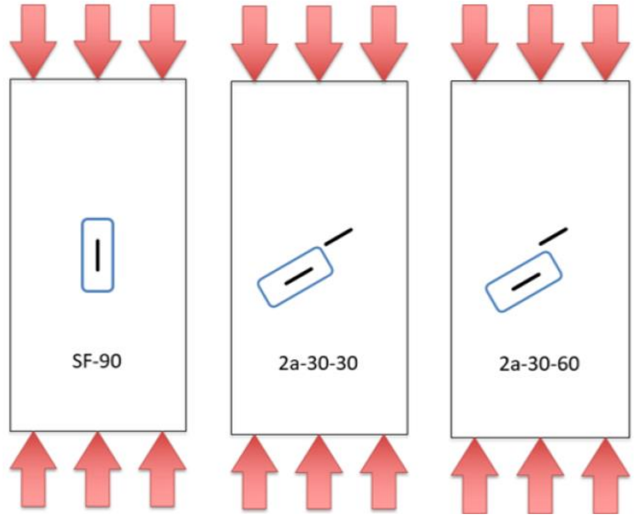

Figure 9 – Schematics of tested flaw geometries. All specimens had horizontal bedding planes ($\psi = 0°$) and were subjected to a constant 3.5 MPa of uniaxial compressive load throughout pressurization. Left: single vertical flaw. Middle: stepped flaw geometry with shallower bridging angle. Right: stepped flaw geometry with steeper bridging angle.

3.1. SF-90

The data collected from the single flaw (SF-90) experiment are shown in Figure 10. The pump pressure is the red curve, internal flaw pressure the green curve, and injected volume the blue curve. Black triangles indicate where sketches were taken as described in 2.2.d. Analysis. The pressure was increased in 0.5 MPa increments and held for 1-2 minutes at each step. The breakdown pressure of the specimen was 3.53 MPa after the injection of 0.11 cm3 of hydraulic fluid. As observed, the breakdown in this case occurred when reaching the target pressure of 3.53 MPa. This was not always the case; the two other experiments run with the same flaw geometry failed during the pressure holding phase. Right now, we do not have a complete explanation for this difference. It might indicate a time dependency or possible small incremental pressure increases from the system while holding (an example of fracturing during the holding phase is shown in the next test example).

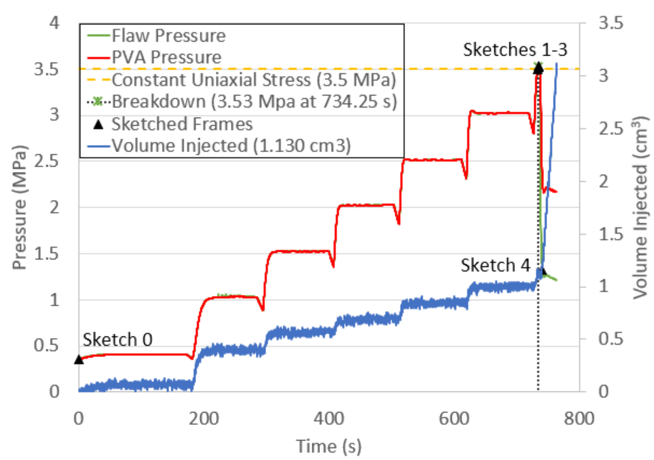

Figure 10 – Pressure and volume data acquired for the SF-90 hydraulic fracture experiment.

The final sketch (Sketch 4) of the produced hydraulic fractures is shown in Figure 11 and the entire crack process is summarized as follows: Crack A(T) initiated first followed by B(T). A(T) propagated past the top seal boundary, causing the internal flaw pressure to slightly drop. About 1 second later, B(T) propagated past the bottom seal boundary. Then both fractures continued propagating outside the seal boundary with a dramatic drop in pressure. The final extent of fracture propagation is shown in Figure 11, and the total propagation time since passing the flaw seal boundary was 6.5 seconds.

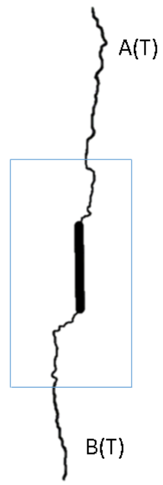

Figure 11 – Final sketch of hydraulic fracture experiment for SF-90. The flaw is 9 mm long and 0.7 mm wide. The flaw seal boundary is indicated by the blue box.

The overall behavior is shown in Figure 11 with fractures propagating up and down, parallel to the applied uniaxial load. Also, the initiation points at the middle of the top and bottom flaw tips were to be expected given the tensile stresses at these locations caused by the uniaxial stresses. This behavior was observed for all three tested specimens with this geometry. A subtle but key observation is the fine-scale meandering of the fractures. Recall that the tested specimens have horizontal bedding planes, and every location where the fracture kinks is where a hydraulic fracture tip reaches a bedding plane.

3.2. 2a-30-30

This next geometry tested is a stepped flaw with a shallow bridging angle ($\alpha = 30°$). It is analogous to the field case of a hydraulic fracture approaching a non-pressurized natural fracture. The test data collected are shown in Figure 12. The breakdown pressure was 4.01 MPa after injecting 0.22 cm3 of hydraulic fluid. In this case, the breakdown occurred during pressure holding.

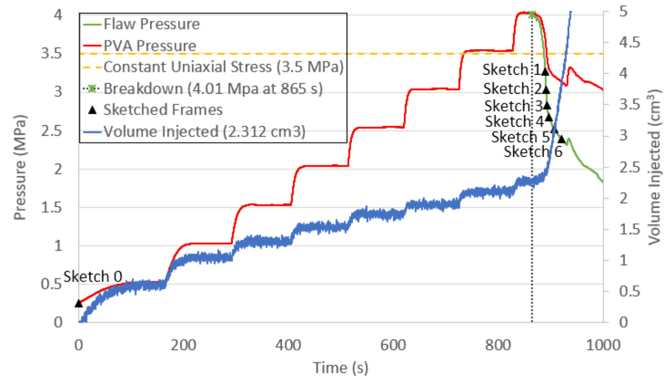

Figure 12 – Pressure and volume data acquired for the 2a-30-30 hydraulic fracture experiment.

The final sketch (Sketch 6) of the produced hydraulic fractures is shown in Figure 13, and the entire crack process is summarized as follows: Tensile cracks A(T) and B(T) initiated almost simultaneously. Tensile crack A(T) propagated past the flaw seal boundary first, and then B(T) propagated past the flaw seal boundary. Both cracks continued propagating until B(T) was arrested. Finally, A(T) ceased propagating, and no new cracks initiated.

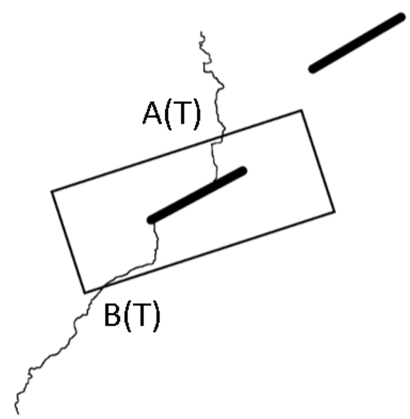

Figure 13 – Final sketch of the hydraulic fracture experiment for 2a-30-30. The flaw seal boundary is indicated by the box.

Similar to the previous test, fine-scale meandering of the hydraulic fractures occurs here. This is especially apparent in A(T). After it propagates outside the seal boundary, whenever its path kinks from vertical to deviated, and sometimes horizontal, this corresponds to the hydraulic fracture tip reaching a bedding plane. This kinking behavior was observed in all three 2a-30-30 experiments. Moreover, the initiation points of A(T) and B(T) on the flaw surface were offset from the flaw tips caused by a combination of the effects of bedding planes and stress concentration from the uniaxial stress. A(T) happens to be significantly more offset because a bedding plane intersects the flaw at that exact location. The offset in initiation points occurred for all hydraulic fractures in the three 2a-30-30 experiments. Finally, as clearly seen, there was no coalescence between the pressurized flaw and the non-pressurized flaw. This was also the case for the other two 2a-30-30 experiments. Overall, the behavior of A(T) was that of a crack propagating perpendicularly to the minimum principal stress and was unaffected by the stress field of the non-pressurized flaw; B(T) started off in a similar way but deviated possibly because of the influence of the bedding planes.

3.3. 2a-30-60

The final test was with the stepped flaw with steeper bridging angle ($\alpha = 60°$). The test data collected are shown in Figure 14. The breakdown pressure was 3.53 MPa after injecting 0.24 cm3 of hydraulic fluid.

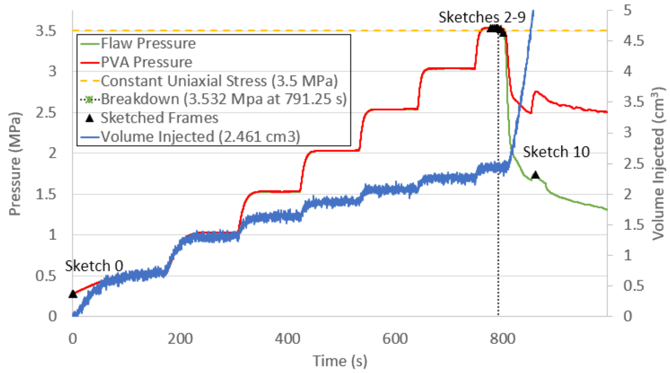

Figure 14 – Pressure and volume data acquired for the 2a-30-60 hydraulic fracture experiment.

The final sketch (Sketch 6) of the produced hydraulic fractures is shown in Figure 15. Tensile crack A(T) initiated during the non-pressurized saturation phase, possibly due to local damage incurred by flaw cutting and by the fact that it happens to be an intersection point of a bedding plane with the flaw. Tensile crack B(T) initiated at the beginning of the pressurization phase, and its location also coincides with a bedding plane intersecting the flaw. Note that crack initiation refers to the start of crack opening before propagation. Propagation only occurs after reaching and holding the pressure of 3.5 MPa and is summarized below.

First, A(T) propagated slightly and temporarily arrested at a bedding plane, followed by B(T) propagating to the flaw seal boundary. Note that the horizontal kink in B(T) within the flaw seal boundary corresponds to a bedding plane, which offset B(T)'s vertical propagation prior to reaching the seal boundary. A(T) continued propagating to the flaw seal boundary while B(T) was propagating vertically outside. Both cracks A(T) and B(T) continued propagating vertically outside the flaw seal boundary until B(T) propagated vertically up the right boundary of an elongated ellipsoidal fossil. B(T) then propagated around it, and once the entire fossil boundary was fractured, B(T) continued propagating up from the top of the fossil. Crack C(T) then branched off of B(T) horizontally through a bedding plane and then kinked up vertically, kinking along the way until it coalesced with the non-pressurized flaw. A(T) continued propagating downward throughout all this and finally arrested.

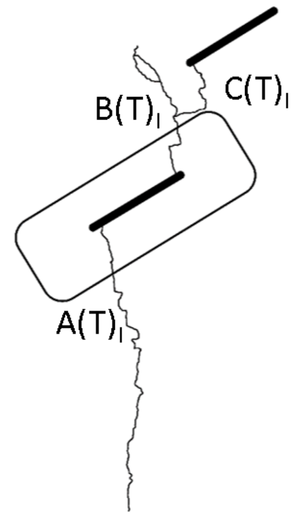

Figure 15 – Final sketch of the hydraulic fracture experiment for 2a-30-60. The flaw seal boundary is indicated by the box.

Hence, this test again displays the kinking behavior at bedding planes as well as some offset fractures. This kinking behavior was observed in all three 2a-30-60 experiments. Moreover, the initiation points of A(T) and B(T) were offset from the flaw tips. This could be due to the bedding planes coinciding with the flaw at these locations but could also be because of the tensile stress concentrations around the flaw tips as shown by Gonçalves da Silva (2014). This experiment also shows the interaction of a hydraulic fracture with a localized heterogeneity, which commonly occur in shallow marine depositional environments. The fracture that propagated around the fossil, B(T), was found to be a single fracture on the rear face of the specimen when examined after the experiment. Similar behavior was observed in one other specimen (not shown) of the same flaw geometry which had a fossil near the flaw. Finally, in all three tests with the 2a-30-60 geometry, the pressurized flaw coalesced with the non-pressurized flaw. Very importantly, however, the coalescence pattern was complex for all tests due to the effects of bedding planes, where the hydraulic fracture always propagated along a bedding plane before coalescing with the non-pressurized flaw.

The details of all the experiments (three for each geometry) along with each sketch as well as photographs are documented in AlDajani (2017).

3.4. Crack Tip and Liquid Front

One final observation, which was consistent for all tested specimens and all flaw configurations, was the observed fluid lag between the advancing crack tip and its driving hydraulic fluid. Examples of this are shown in Figure 16, where the crack tip is ahead of the liquid front. The hydraulic fracture propagation behavior in shale, as observed in the recorded high-speed video, is a cycle of fracture tip advancement, fluid catching up with the advanced fracture tip, crack tip advancement again, and repeated in incremental steps.

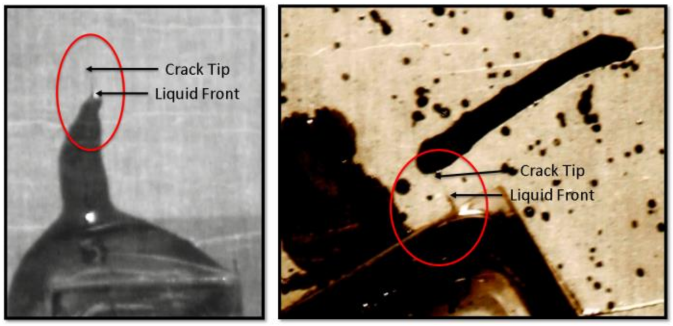

Figure 16 – Examples of observed fluid lag, where the crack tip is ahead of liquid front. Left: SF-90. Right: 2a-30-60.

4. CONCLUSIONS

The objective of this paper was to present the design of a hydraulic fracture experiment that allows one to visually capture the fracture behavior in a controlled laboratory setting to gain a fundamental understanding of the mechanisms underlying the hydraulic fracture processes in shales.

This novel experimental setup was designed to pressurize an individual flaw of a specimen subjected to uniaxial stress, record pressure and volume throughout pressurization and fracturing, and visually capture high-resolution and high-speed images of the observed behavior. A new flaw pressurization device was designed and fabricated at MIT, which allows us to investigate hydraulic fracturing of various flaw configurations and loading conditions.

Prismatic Opalinus Shale specimens with three pre-existing flaw geometries were tested, namely a single flaw and two double flaw geometries. The single flaw experiment showed that the flaw pressurization device was able to produce a hydraulic fracture and how the fractures propagated in shale.

In the case of the stepped flaw geometries, all the 2a-30-30 specimens had no coalescence between the pressurized flaw and the non-pressurized flaw. However, in all 2a-30-60 specimens, the two flaws coalesced. For all of these, the fracture propagation path meandered and kinked whenever it encountered a bedding plane.

In all tests, these experiments show a lag between fracture tip and fluid front. They also gave insight into how hydraulic fractures propagate in shales through incremental advancing steps rather than one continuous, smooth, advancement.

ACKNOWLEDGEMENTS

The authors would like to acknowledge the support of this research by TOTAL in the context of the project Multi-scale Shale Gas Collaboratory. We not only received financial support but were helped through many constructive discussions with out technical contacts. We also would like to acknowledge the Underground Research Laboratory in Mont Terri, Switzerland which provided the shale core borings used for this study.

REFERENCES

1. AlDajani, O. A. 2017. Fracture and hydraulic fracture initiation, propagation and coalescence in shale. *Master's thesis, Massachusetts Institute of Technology*.
2. AlDajani, O. A., S. P. Morgan, J. T. Germaine, and H. H. Einstein. 2017. Vaca Muerta Shale – Basic Properties, Specimen Preparation, and Fracture Processes. In *Proceedings of the 51st U.S. Rock Mechanics/Geomechanics Symposium, San Francisco, California, USA, 25 – 28 June 2017*.
3. Bobet, A. 1997. Fracture coalescence in rock materials: experimental observations and numerical predictions. *Doctoral dissertation, Massachusetts Institute of Technology*.
4. Gonçalves da Silva, B. M. 2009. Modeling of crack initiation, propagation and coalescence in rocks. *Master's thesis, Massachusetts Institute of Technology*.
5. Gonçalves da Silva, B. M. and H. H. Einstein. 2014. Finite element study of fracture initiation in flaws subject to internal fluid pressure and vertical stress. *International Journal of Solids and Structures*. 51(23-24): 4122-4136.
6. Gonçalves da Silva, B. M. 2016. Fracturing processes and induced seismicity due to the hydraulic fracturing of rocks. *Doctoral dissertation, Massachusetts Institute of Technology*.
7. Miller, J. T. 2008. Crack coalescence in granite. *Master's thesis, Massachusetts Institute of Technology*.
8. Morgan, S. P. 2015. An experimental and numerical study on the fracturing processes in Opalinus shale. *Doctoral dissertation, Massachusetts Institute of Technology*.
9. Reyes, O. M. L. 1991. Experimental study and analytical modelling of compressive fracture in brittle materials. *Doctoral dissertation, Massachusetts Institute of Technology*.
10. Wong, L. N. Y. 2008 Crack coalescence in molded gypsum and Carrara marble. *Doctoral dissertation, Massachusetts Institute of Technology*.